Nano Energy 81 (2021) 105643

Contents lists available at ScienceDirect

Nano Energy

journal homepage: http://www.elsevier.com/locate/nanoen

Rational design of interlayer binding towards highly reversible anion intercalation cathode for dual ion batteries

Maiwen Zhang, Yi Pei, Wenwen Liu, Ruilin Liang, Ya-Ping Deng, Zhongwei Chen, Aiping Yu *

Department of Chemical Engineering, Waterloo Institute for Nanotechnology, University of Waterloo, ON N2L 3G1, Canada

ARTICLE INFO

Keywords:
Dual ion batteries
Anion intercalation
Graphite intercalation compounds
Rational-designed cathodes
Interlayer bonding

ABSTRACT

Dual ion batteries are one of the emerging substitutes for lithium ion batteries with high operating voltages and energy density, but their recent advancements have been limited by unsatisfactory cathode stability in the form of irreversible exfoliation. To address this bottleneck, a strategy to selectively incorporate carboxylic anhydride functionality between graphite layers is developed to enforce a stabilizing effect to the crystal structure, which allows for effective performance optimization through particles downsizing and interlayer distance tuning without the compromises of intercalation site disruption and voltage deduction. The resulting graphite cathode experienced significant capacity, rate capability and stability improvements, achieving a highly reversible capacity of 91.2 mAh g^{-1} at 2 C, which then cycled consistently for over 1,000 cycles. Overall, this work removes a major handicap that has limited the development of dual ion batteries and demonstrates a design pathway for high performance graphite intercalation cathode suitable for anion intercalation with both enhanced stability and discharge capacity.

1. Introduction

Safety concerns, material supply inconsistency and energy density limitation of traditional lithium ion batteries (LIBs) have motivated the development of next generation energy storage devices [1–6]. Among the emerging systems, dual ion batteries (DIBs) have attracted immense attentions as probable replacement with comparable or even better performances [7–11]. Unlike traditional LIBs that operate solely based on cation shuttling, both cations (Li^+, Na^+, K^+) and anions (PF_6^-, $TFSI^-$) de/intercalation in corresponding electrode are enabled in DIBs [12,13]. Specifically, anion intercalation to cathode and cations insertion into anode occur when the batteries are charged, while anions and cations are extracted to electrolyte in the discharge process [14]. Under such mechanism, DIBs not only present a high discharge voltage (up to 6.0 V) [15], but also high theoretical energy density [16]. However, despite the promises, restrictions associated with anions insertion inevitably lead to capacity and life span limitations [12,14]. In contrary to alkali-ion batteries that utilizes transition metal oxides as the framework of alkali-ion (Li, Na, K with the radius within 0.76–1.38 Å) diffusion, molecular-size anions (3–4 Å) can only be shuttle within cathode materials containing large tunnels such as polyanionic compound and 2D graphite intercalation compounds (GICs) [17–20]. Given so, development of suitable cathode materials has been one of the most important challenges in the field of DIBs.

Previous reports have identified that both ex/intercalation and surface redox processes occur in GICs; the ex/intercalation reaction is shown to be beneficial for high redox potential, and the surface redox processes provide additional capacity in lower voltage ranges [16,21,22]. However, the anion ex/intercalation reaction is both thermodynamically and kinetically hindered by insufficient interlayer distances (~3.5 Å), while the surface redox processes are primarily controlled by the available active sites on the material surface [23]. Previous studies have reported that battery capacity and rate capability can be improved by lowering particle size to increase surface area [24–26]. Some notable examples adapting this approach include 3D porous microcrystalline carbon and nanoflake constructed porous graphite [27–29]. Nevertheless, such strategies are generally accompanied with the compromise of intensified interlayer exfoliation or surface corrosion, which are not ideal for achieving optimal electrochemical performance with GICs. Under such circumstances, surface modification may be considered as an effective method to both increase the applicable active sites for capacity improvement and lower the interphase resistance of ex/intercalation reaction.

Herein, we aim to accommodate the instability of graphite during

* Corresponding author.
E-mail address: aipingyu@uwaterloo.ca (A. Yu).

https://doi.org/10.1016/j.nanoen.2020.105643
Received 19 October 2020; Received in revised form 16 November 2020; Accepted 25 November 2020
Available online 17 December 2020

repetitive anion de/intercalation through surface modification. In departure from previous strategies that have little influence to the stacking of graphite layer, we demonstrate that the graphite interlayer interaction can be strengthened with induced formation of surface carboxylic anhydride functionality, which effectively suppress interlayer exfoliation upon cycling. As shown in Fig. 1, through a surface functionalization strategy under high-pressure treatment, micron-sized graphite particles are reduced to smaller particles with increased surface area, while maintaining the carbon layer-stacking as a result of the incorporated function groups. Such configuration not only enlarges the interlayer distance which is beneficial for cation insertion, but also prevents interlayer separation during cycling. Benefiting from these specific properties, the graphite cathode that undergone the optimal functionalization process achieves a highly reversible capacity of 91.2 mAh g^{-1} at 2 C and capacity retention of 80% after 1,000 cycles of operation.

2. Results and discussion

2.1. Structural and surface characteristics

Surface functionalization of graphite was carried out using high-pressure ball-milling with and without the addition of dry ice, details of the synthetic process are provided in the methods section. Dry ice was particularly selected to provide high CO_2 pressure in the ball-milling chamber to promote the formation of edge carboxylation on the graphite particle [30], the process is chosen to effectively functionalize the graphite cathode owing to its eco-friendly, low cost, easiness operation and huge potential suitable for large-scale production [31]. The pristine and treated samples are labeled as GP, GP 1-0, GP 1-4 and GP 1-8 respectively, with the number representing the mass ratio of GP to dry ice added to the ball-milling chamber. Atomic stacking of each sample was first evaluated by X-Ray diffraction (XRD), and the (002) reflection located at around 26.5° was used to investigate the interlayer distance along c axis. As revealed in Fig. 2**a**, all treated samples show slightly increased c value compared to the untreated GP sample, suggesting interlayer expansion as a result of the ball-milling treatment. Morphology changes of the samples observed with scanning electron microscopy (SEM, Fig. S1) identifies gradual reduction of particle sizes with increasing CO_2 amount, from over 10 μm of the pristine GP to around 3 μm in GP 1-8. The size reduction is due to the higher CO_2 pressure environment that promotes the C–C bond breaking of graphite particle [31]. As for their gas adsorption Brunauer-Emmett-Teller (BET) surface area analysis (Figs. S2 and 2**b**), the untreated GP demonstrates a low surface area of 25 m^2 g^{-1} and the values for GP 1-0 and GP 1-4 are increased to 272 m^2 g^{-1} and 422 m^2 g^{-1} after ball milling, which is probably associated with both reduced particle size. However, despite having the smallest particle size, surface area of GP 1-8 did not further increase but instead reduce to 374 m^2g^{-1}, suggesting a surface condition that differs from the other samples, which will be analyzed in later section. Turning to the Raman measurements, a strong G band and minimal D band located at 1,576 cm^{-1} and 1,345 cm^{-1} are observed in the spectra of GP (Fig. 2**c**), indicating negligible amount of edge distortions and topological defect [32]. Upon ball-milling, relative D band intensity of all treated samples significantly increases due to the generation of crystallographic defects by size reduction, with GP 1-4 exhibiting the largest I_D/I_G ratio of 0.94. Noted that the trend of I_D/I_G ratio changes from GP 1-4 to GP 1-8 (I_D/I_G ratio of 0.65) also align with the BET results, which leads to a hypothesis that on top of the reduced particle sizes, a different modification mechanism has been triggered under higher CO_2 concentration ball-milling, leading to an alternative surface conditions.

To identify the surface condition of the samples, Fourier transform infrared (FT-IR) spectroscopy was employed to investigate their surface functionalities. All samples display a weak sp^3 C–H peak at 2,921 cm^{-1} associated with defects on the carbon layer, a sp^2 carbon peak at 2,840 cm^{-1} and a strong broad peaks at 3,440 cm^{-1}~3,500 cm^{-1} corresponding to vibration mode of residual crystal water in the specimen (Fig. S3) [30]. Upon the addition of dry ice in the ball-milling process of GP 1-4, occurrence of edge-carboxylation is evidenced by a strong C═O stretching peak at 1,720 cm^{-1} and a weak C–O stretching peak at 1, 210 cm^{-1} from O═C–OH [31]. While in the FT-IR spectrum of GP 1-8, apart from the distorted carboxyl acid peaks (1,707 cm^{-1} and 1, 272 cm^{-1} for the C═O and C–O bonds, respectively), new adsorptions exclusively associated with carboxylic anhydride functionality have emerged [33–36]. These include a pair of new absorptions at 1,837 and 1,762 cm^{-1} commonly referred to the asymmetric and symmetric C═O stretching vibrations, and a new peak at 1,090 cm^{-1} from the C–O–C stretching vibration (Fig. 2**d**). The surface functional groups were

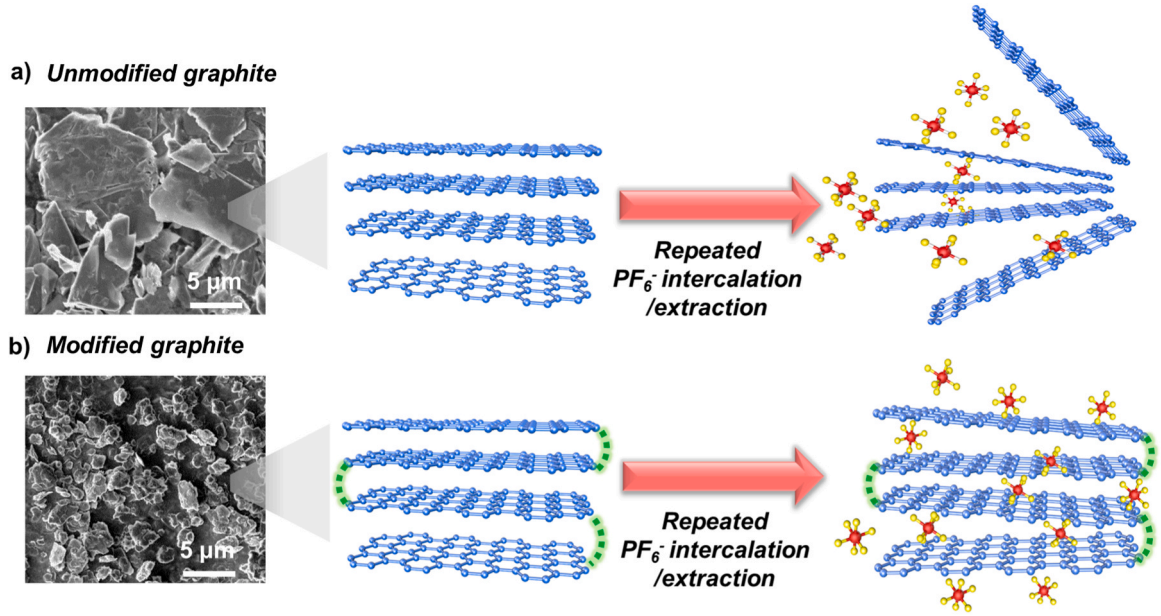

Fig. 1. SEM images and schematic illustration of working mechanism of a) unmodified graphite and b) modified graphite cathode. Blue, red and yellow spheres represent C, P and F atoms, respectively. The green dashes represent functionalities that enact binding force between crystalline layers. (For interpretation of the references to colour in this figure legend, the reader is referred to the web version of this article.)

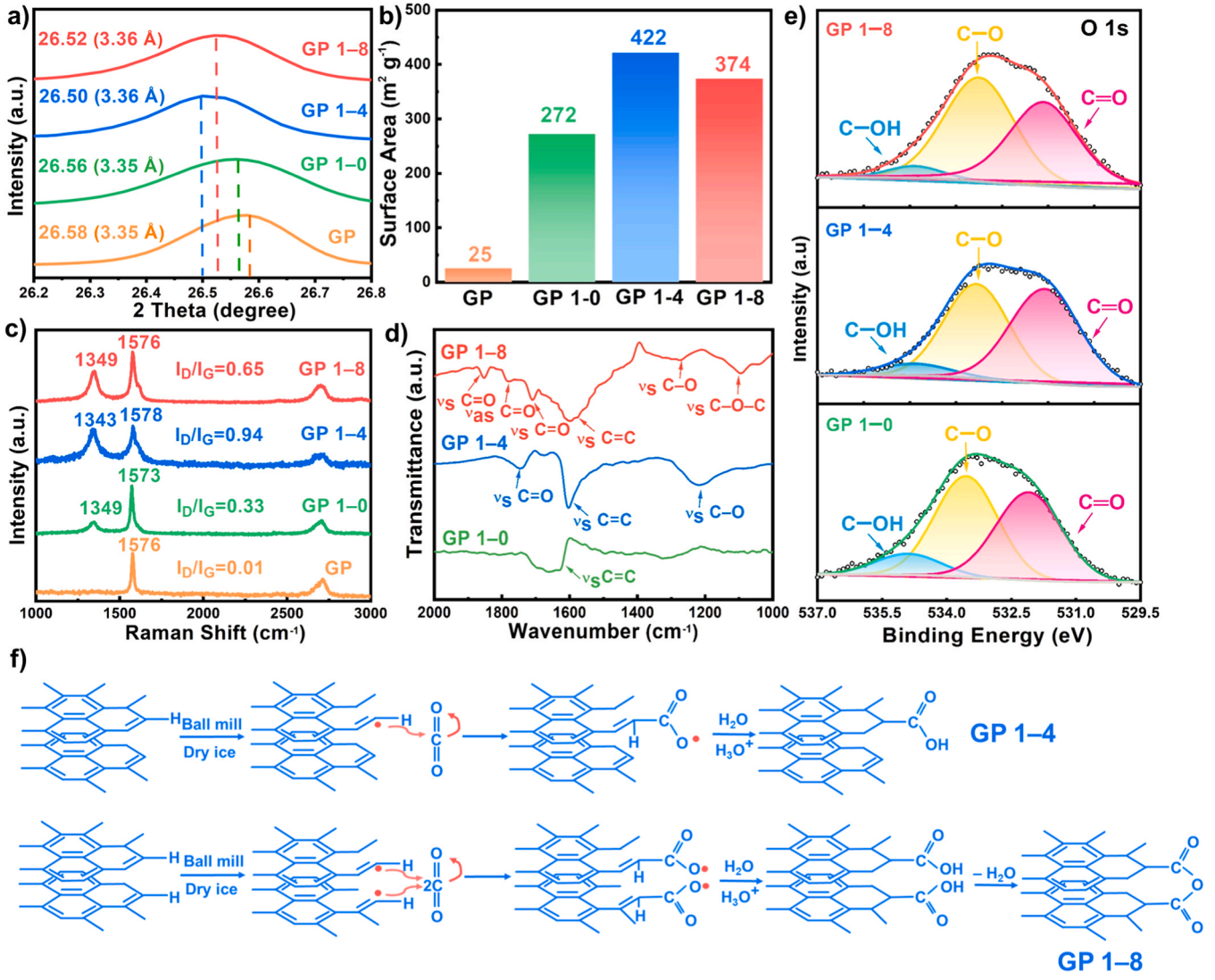

Fig. 2. a) X-Ray diffraction patterns, b) BET surface area data, c) Raman spectra of GP, GP 1-0, GP 1-4 and GP 1-8. d) FT-IR spectra (KBr pellets) and e) XPS spectra of GP 1-0, GP 1-4 and GP 1-8. f) Proposed formation reaction of carboxylic graphite (GP 1-4, first line) and carboxylic anhydride graphite (GP 1-8, second line).

further investigated by X-Ray photoelectron spectroscopy (XPS, Fig. 2**e**), in which the O *1s* spectra of GP 1-0, GP 1-4 and GP 1-8 are deconvoluted into three feature peaks that refer to oxygen ions in C–OH (carbon single bond to the hydroxyl group), C–O (oxygen single bond to carbon) and C═O (oxygen double bond to carbon) at 534.9, 533.5 and 532.1 eV, respectively [37,38]. Quantitative analyses suggest reduced C–OH proportion moving from GP 1-0 to GP 1-4, whereas the ratio of C═O increases (Table S1), signaling the formation of carboxylic acid in GP 1-4. When continue raising the CO_2 concentration in GP 1-8, the relative intensity of the C–O peak largely increases, accompanied by reduction of the C–OH ratio and minimal changes of the C═O peak. Combining with the FT-IR results, this likely implies the occurrence of carboxylic acids on the graphite surface undergoing a condensation reaction to form carboxylic anhydride functionality. Based on the above results, it can be concluded that two separate reactions have been triggered in the ball-milling process: the first is the edge/surface carboxylation on the graphite, and the second is the condensation of carboxyl group to carboxylic anhydride moiety that is activated by the specific condition of high CO_2 pressure (Fig. 2**f**).

The above identified surface functionalization mechanism is in good agreement with the trends observed in the physical characterization process. Specifically, the formation of carboxylic anhydride functionality between neighbouring carbon layer provides binding strength that limits the expansion and subsequent separation of the layer. This explains the higher peak location of GP 1-8 (26.52°) compared to GP 1-4 (26.50°), and their lower BET surface area despite smaller particles sizes [39]. Additionally, this specific functionality and carbon layer arrangement restricts the exposure of inner layer carbon from further reaction, resulting in reduced abundancy of defects and thus lower I_D/I_G ratio (0.65) compared to that of GP 1-4 (0.94) [30,31]. Overall, it can be concluded that the high CO_2 concentration ball-milling condition enables effective down-sizing of graphite particles while suppressing vast generation of defects in the carbon crystal structure.

2.2. *Functionality and electrochemical behavior correlation*

Galvanostatic charge/discharge and cycling voltammetry (CV) were conducted using 4 M $LiPF_6$/EMC electrolyte and Li metal as counter electrode to investigate the electrochemical behavior after surface functionalization. High $LiPF_6$ concentration was provided to ensure presence of sufficient electrolyte ionic conductors throughout the cycling process [15]. As shown in Fig. 3**a**, GP exhibits typical characteristics of DIBs cathode with two discharge platforms located at 4.65 V and 4.25 V that contribute a total capacity of 76 mAh g^{-1}, corresponding to two stages of anion intercalation process [25,40]. For the ball milled GP 1-0, it experiences clear voltage and capacity reductions for

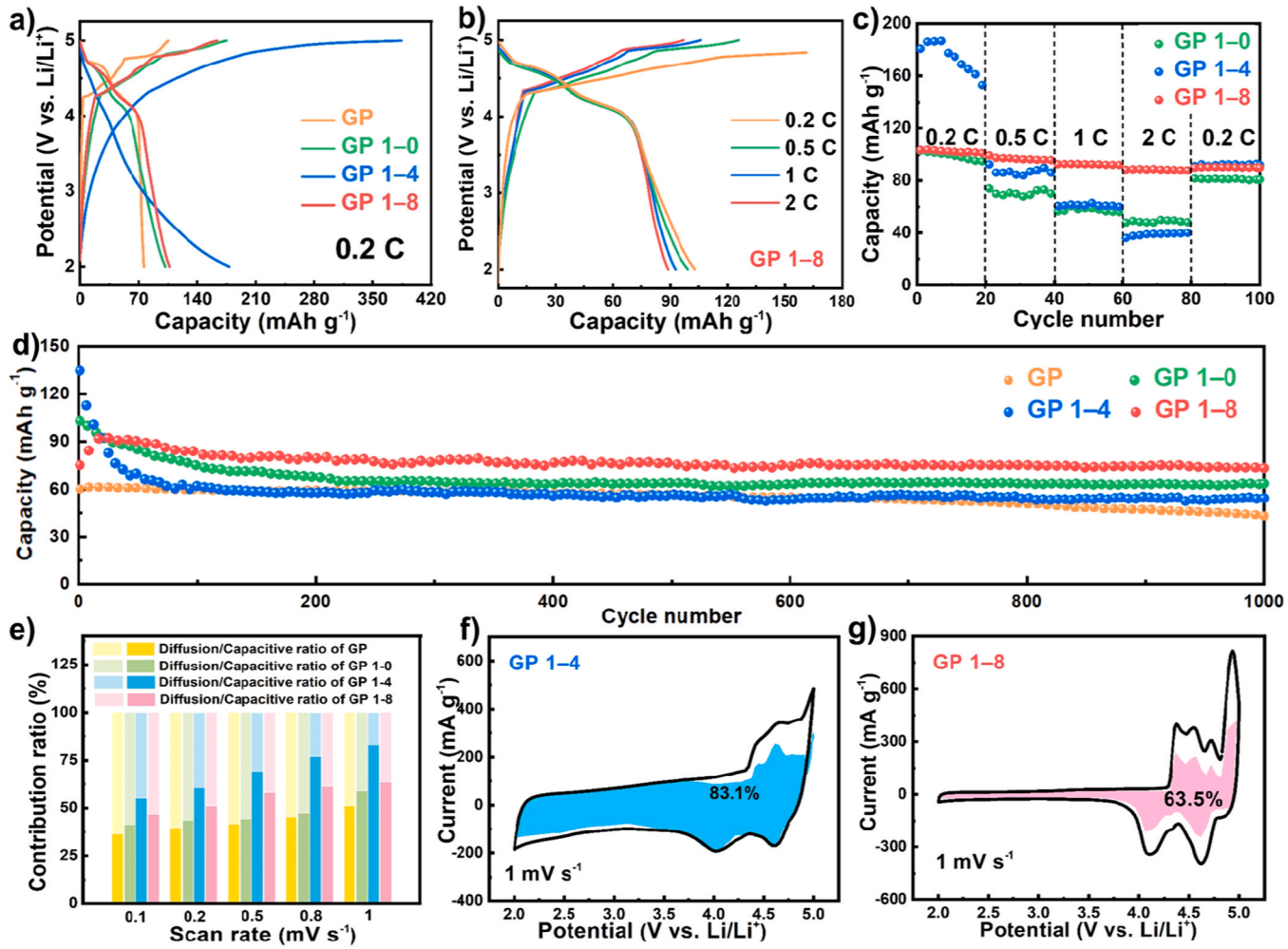

Fig. 3. Galvanostatic charge–discharge curves of a) GP, GP 1-0, GP 1-4 and GP 1-8 at 0.2 C, b) GP 1-8 at 0.2 C, 0.5 C, 1 C and 2 C. c) Rate capabilities of GP 1-0, GP 1-4 and GP 1-8. d) Long term cycling results of GP, GP 1-0, GP 1-4 and GP 1-8. e) Contribution ratio of the capacitive (bottom color) and diffusion controlled (top color) capacity at different scan rates of GP, GP 1-0, GP 1-4 and GP 1-8. f)–g) Capacitive contribution of GP 1-4 and GP 1-8 at 1 mV s^{-1}. (For interpretation of the references to colour in this figure legend, the reader is referred to the web version of this article.)

these two platforms, likely due to shifts from a two-phase reaction into a solid solution reaction. It also gains additional discharge capacity in the range of 4.0–2.0 V associated with increased surface-redox reactions provided by enlarged surface area. Voltage declines of the two anion intercalation platforms become more severe when small amount of CO_2 is used for GP 1-4, as the two intercalation plateaus are essentially replaced with a slopping discharge curve. This aligns with its further increased surface area and enlarged interlayer spacing caused by carboxyl groups formation, which disrupts anion intercalation but facilitates additional surface electrochemical reactions [30]. The lowered first cycle Coulombic efficiency in GP 1-8 (64%) compared to GP (72%) is likely due to its increased surface area, which provides additional sites for electrolyte decomposition and surface interphase formation at the initial stage [41,42]. The functional groups on the surface of GP 1-8 may also promote electrolyte decomposition [43]. Interestingly, the two intercalation platforms at 4.65 V and 4.25 V reappear in the charge-discharge profile of GP 1-8 with insignificant voltage changes and the material achieves a total capacity 37% higher compare to the pristine GP. The results indicate the down-sizing of GP 1-8 by high CO_2 concentration ball-milling effectively improves its available capacity without changing its primary energy storage mechanism, which remains to be an intercalation dominant process. This is critical, as capacity increments that cause substantial voltage deduction will not yield meaningful improvement in battery energy density.

In the ensuing rate capability tests, GP 1-8 achieves capacities of 103.8, 99.3, 92.7, and 88.8 mAh g^{-1} at 0.2 C, 0.5 C, 1 C and 2 C, respectively, with minimal voltage decreases for the primary discharge platforms (Fig. 3**b** and **c**). In contrast, capacity of the other ball-milled samples first experience substantial decays in the 0.2 C cycles, likely due to structural exfoliation and incomplete anion extraction from high capacity utilization, and then further reduce by over 40% when the rate is raised to 2 C (Fig. S4). GP 1-8 also outperforms all samples in long period cycling at 2 C with the highest reversible capacity of 91.2 mAh g^{-1} and capacity retention of over 80% after 1,000 cycles of operations, whereas GP 1-0 and GP 1-4 retained only 62% and 42% of their capacity in the same duration (Fig. 3**d**). The capacity increase of GP 1-8 in the initial cycles can be attributed to the gradual wetting and activation process of the electrode [25]. The same trend is not observed on GP 1-0 and GP 1-4, because they experience significant capacity decade due to structural exfoliation by repeated anion intercalation/extraction that outweigh the gain from the activation process [7,22]. These performance comparisons demonstrate the advantages of GP 1-8 by achieving an optimal balance between surface area and surface functionalities. The relatively high surface area enables better site availability, while the carboxylic anhydride functionality provides the necessary binding strength to ensure long term integrity of the material structures. Worth noting, these performance of GP 1-8 is superior when compared to results reported in previous literatures [7,44–46]. Redox

behavior and electrochemical kinetics investigations on the graphite cathodes by CV analyses reveal gradual weakening of redox peak distinctiveness and transition toward surface-dominate processes when shifting from pristine GP to GP 1-0 then to GP 1-4 (Figs. S5 and S6) [47–49], which matches the increasing trends in crystal logical defects and surface area of the samples. As for GP 1-8, despite having a significant portion of its capacity being surface-controlled, it exhibits much less capacitive characteristics and more recognizable redox peaks compare to GP 1-4, verifying again its intercalation dominant nature. This is also supported by quantitative analyses of the CV curves, which show large increases in diffusion-controlled processes when moving from GP 1-4 to GP 1-8 (Figs. 3**e** and S7). For instance, at the scan rate of 1 mV s^{-1}, only less than 17% of the capacity demonstrated by GP 1-4 is diffusion-controlled (Fig. 3**f**), while over 30% of the energy storage process in GP 1-8 with smaller particle size are independent of the available surfaces (Fig. 3**g**). Additionally, electrochemical impedance spectroscopy (EIS) analysis suggests GP 1-8 exhibits the lowest charge-transfer impedance evidenced by the smallest semicircle at high-frequency regime, whereas the GP 1-4 presents a very steep slope in low-frequency region that is associated with the fast reaction kinetic of capacitive behaviors (Fig. S8) [50].

2.3. *Ex-situ* mechanism investigations

To reveal the mechanistic variations of the ball-milled samples with different functional groups, *ex-situ* XRD and Raman analysis were employed at various selected states of charge/discharge. As shown in Fig. 4**a**, during the initial charging to 4.5 V, the (002) peak of GP 1-8 shifts distinctly to lower angle, followed by widening and further left shift at 4.8 V and 5.0 V, indicating the intercalation of PF_6^- anions that expands the d-spacing of the carbon layer graphite. The total shift from the initial state to 5.0 V is ~2.6°. When discharged, the (002) peak gradually narrows and moves to a peak position that is slightly left shifted by 0.7° compared to its initial state, indicating the PF_6^- de-intercalation from graphite. Among the three ball-milled samples, GP 1-8 experienced the smallest peak shift, which is in good consistent with its best cycling performance (Fig. S9). For comparison, GP 1-4 shows a (002) peak shift of over 6.0° when charged to 5.0 V and a large shift of 2° when discharged, which are clear signs of irreversible change occurrence in the graphite likely through complete exfoliation of carbon layers [51]. As for GP 1-0, its (002) peak also experienced significant widening and left shift as it was charged, when discharged, the peak shows a smaller but still significant shift of over 0.8°.

As for the *ex-situ* Raman spectroscopy, anion intercalation has been reported to break the interlayer stacking of graphite, both physically and electronically due to repulsion of the intercalate molecule, causing the G

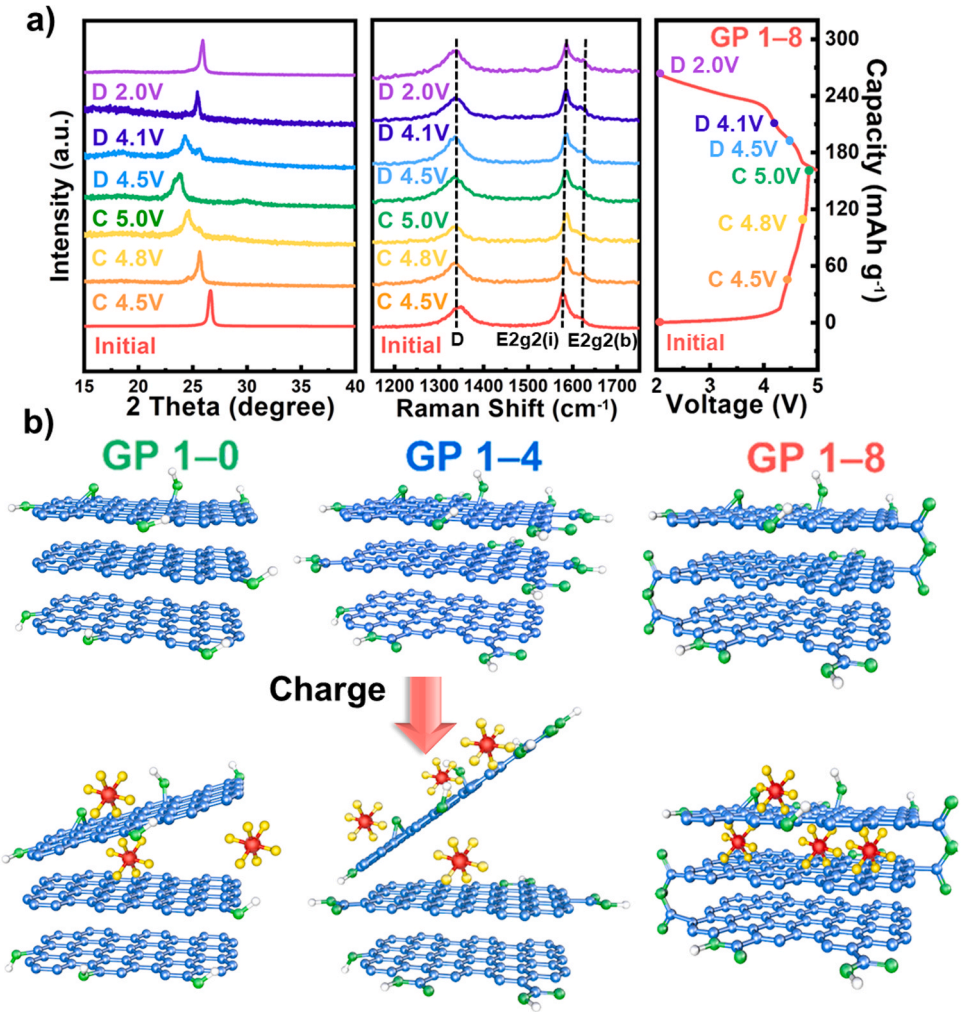

Fig. 4. a) *Ex-situ* XRD and Raman measurements of GP 1-8 at the current density of 0.2 C at different charge/discharge potential. b) Charging mechanisms of GP 1-0, GP 1-4 and GP 1-8. Blue, green, red, yellow and white spheres represent C, O, P, F and H atoms. (For interpretation of the references to colour in this figure legend, the reader is referred to the web version of this article.)

band (~1,575 cm^{-1}) to split into the doublet peak of E_{2g2}(i) mode and E_{2g2}(b) mode [52]. The E_{2g2}(i) mode is vibrations of the carbon atoms not affected by the intercalated planes, while the E_{2g2}(b) mode originates from vibrations of carbon atoms adjacent to the layers of the intercalated planes. Intensity ratio (I_i/I_b) of the two doublets can therefore provide qualitative insights to the level of intercalation as well as the degree of irreversible changes caused by the process [53,54]. From the results, it is clear that after a single cycle of charge/discharge, the E_{2g2}(i) peak of GP 1-0 is significantly weakened, while its E_{2g2}(b) peak appears and drastically increases in intensity (Fig. S9a, Table S2). As a result, its I_i/I_b ratio reduces from 4.08 to 1.66, signifying drastic changes in its crystal symmetry as a result of the intercalation. As for GP 1-4, its I_i/I_b ratio is relatively low to begin with, indicating disrupted symmetry due to presence of abundant carboxyl functionality. Its crystal symmetry is further broken by the intercalation process, as its E_{2g2}(i) peak reduces in distinctiveness, causing its I_i/I_b ratio to reduce from 1.9 to 1.45 (Fig. S9b, Table S2). In contrast, while GP 1-8 also experience E_{2g2}(i) reduction and E_{2g2}(b) growth during the charging process, it demonstrates much better recovery after the discharge with its final I_i/I_b ratio being 1.93 versus the 2.72 of its initial state (Fig. 4**a**, Table S2). This showcases the strong resilience of GP 1-8 toward the volume changes and symmetry disruption applied by the anion intercalation process. Additionally, the I_D/I_G ratio of GP 1-8 only changes from the initial 0.65–0.84 after a complete cycle, both the final value and value changes are the smallest among all test samples, demonstrating that GP 1-8 has the least defects as a result of the intercalation process, and confirm once again that it has the highest structural robustness among all samples.

Based on the above findings, a scheme of GP 1-0, GP 1-4 and GP 1-8 and their carbon layer variation during anion intercalation are illustrated in Fig. 4**b**. As shown, the mechanic ball-milling processes incorporate defects and primarily hydroxyl groups to GP 1-0; electrochemical behavior of the sample does not vary significantly as a result, aside for gaining small amount of capacitive contribution due to additional exposed surface. For GP 1-4, high abundancy of carboxylic acid is generated with the addition of CO_2 to the process, which causes weakening of the Van der wall forces between the carbon layer, making them much more susceptible to exfoliation caused by intercalation. Lastly, in GP 1-8, the increment in CO_2 concentration does not lead to further carbon layer separation, instead the high concentration promoted the conversion of the carboxyl group to carboxylic anhydride functionality, which in turn provides a binding force that is beneficial to the cycling stability. This specific structure and functional group composition not only facilitates better intercalation kinetic by size reduction, but also prohibits excessive carbon layer exfoliation detrimental to long term battery performance.

3. Methods

3.1. GP ball-milling

In a typical process, the ball-milling of commercial graphite powder was carried out in a ball-mill machine (Nanjing NanDa Instrument Plant) with/without dry ice. To start, 0.5 g of graphite powder (Sigma, natural graphite, 2–15 μm, 99.9995% metals basis, Lot#14735) and 0, 2 or 4 g of dry ice were put into a stainless-steel capsule together with 30 stainless steel balls with diameter of 6 mm. The container was subsequently sealed and fixed in the ball-mill machine and started agitation with 150 rpm for 24 h. The resulting product was then washed by 1 M aqueous HCl solution in order to acidify carboxylates and remove metallic impurities. The resulting product was freeze-dried at − 120 °C for 48 h.

3.2. Material characterization

X-ray diffraction patterns of the samples were obtained by a Rigaku Miniflex 600 X-ray Diffractometer which contains a graphite monochromator and a Cu Kα radiation source (λ = 1.5406 Å). Surface morphology of the materials was observed with a Zeiss ULTRA plus Field Emission Scanning Electron Microscope. Raman spectra of the samples were tested with a Bruker Senterra System using a 532 nm wavelength excitation line. The surface area was investigated by N_2 adsorption-desorption measurements on a Brunauer-Emmett-Teller surface area analyzer (Quantachrome Instruments QuadraSorb SI4). Infrared spectra were recorded by Fourier-transform infrared spectrometer (Spectrum One, Perkin Elmer Instruments Co. Ltd., USA). X-ray photoelectron spectra of the samples were collected using Thermal Scientific K-Alpha X-ray Photoelectron Spectrometer System and the spectra were calibrated with the C–C 1s peak at 284.5 eV.

3.3. Electrochemical characterization

The cathode was prepared by mixing the graphite samples with super P and PVDF with mass ratio of 8:1:1. After mixing in NMP solvent, the slurry was casted onto Al foil and then dried at 80 °C under vacuum overnight. Afterwards, the cathode was cut into circles with diameter of 15 mm, the typical mass loading is 1.5 mg cm^{-2}. Meanwhile, 15 mm circular Li foils are used as anode, with polypropylene separator (Celgard 2400) as separator. Finally, a CR2016 coin cell was assembled with 120 μL of 4 M $LiPF_6$/EMC in argon-filled glove box. The galvanostatic charge/discharge tests (GCD) were conducted on LAND CT2001A and cyclic voltammetry (CV) tests were performed using computer-controlled BioLogic VMP-300 workstation from 2 V to 5 V, respectively.

3.4. Cyclic voltammetry reaction kinetic calculation

The kinetic information was gained based on the relationship between scan rate (v) and current (i) as following [55]:

$$i = av^b \tag{1}$$

where both a and b are constant parameters. If b-value reaches 0.5, the overall process shows a typical battery behavior; a b-value of 1 represents that the current is almost surface-controlled.

The capacitive contribution ratio of the capacity was calculated by isolating the capacitive current from the overall current response i [55]:

$$i = k_1 v + k_2 v^{1/2} \tag{2}$$

where $k_1 v$ and $k_2 v^{1/2}$ represent the capacitive and diffusion-controlled current in the total current at different potentials. By scheming $i/v^{1/2}$ vs. $v^{1/2}$ at different voltages, the ratio of capacitance was calculated.

4. Conclusion

In summary, a novel DIBs graphite cathode modification strategy is proposed that enables effective capacity and rate capability improvement through strengthened carbon layer binding that prevents undesirable exfoliation. It is discovered that hydroxyl and carboxyl acids on graphite lead to significant increment in DIBs capacity, but excessive abundancy of such functional groups encourage carbon layer separation and lead to rapid performance degradation. In comparison, functional group such as carboxylic anhydride formed at the specific ball milling condition of excessive CO_2 concentration can aid the binding of carbon layer, allowing rapid PF_6^- intercalation while maintaining the stability of the graphite crystal structure. Benefiting from the optimized condition, graphite cathode material modified by carboxylic anhydride delivers discharge capacity of 103.8 mAh g^{-1} at 0.2 C and capacity retention of 80% after 1,000 cycles at 2 C. This strategy showed the possibility to reach a desirable compromise between practical capacity and structure stability of GICs through rational surface modification, opening a new avenue to facilitate the commercial application of DIBs.

CRediT authorship contribution statement

Maiwen Zhang: Conceptualization, Methodology, Data curation, Validation, Investigation, Writing - original draft, Writing - review & editing, Visualization. **Yi Pei:** Conceptualization, Methodology, Data curation, Validation, Writing - original draft, Writing - review & editing. **Wenwen Liu:** Writing - original draft, Validation, Writing - review & editing. **Ruilin Liang:** Conceptualization, Data curation, Writing - original draft, Validation, Investigation. **Ya-Ping Deng:** Writing - original draft, Validation, Writing - review & editing. **Zhongwei Chen:** Conceptualization, Methodology, Writing - original draft, Writing - review & editing. **Aiping Yu:** Conceptualization, Methodology, Supervision, Validation, Writing - original draft, Writing - review & editing.

Declaration of Competing Interest

The authors declare that they have no known competing financial interests or personal relationships that could have appeared to influence the work reported in this paper.

Acknowledgment

This work was sponsored by Natural Sciences and Engineering Research Council of Canada (NSERC), University of Waterloo and Waterloo Institute for Nanotechnology.

Appendix A. Supporting information

Supplementary data associated with this article can be found in the online version at doi:10.1016/j.nanoen.2020.105643.

References

[1] J. Fu, R. Liang, G. Liu, A. Yu, Z. Bai, L. Yang, Z. Chen, Recent progress in electrically rechargeable zinc-air batteries, Adv. Mater. 31 (2019), 1805230.
[2] Y.P. Deng, Z.G. Wu, R. Liang, Y. Jiang, D. Luo, A. Yu, Z. Chen, Layer-based heterostructured cathodes for lithium-ion and sodium-ion batteries, Adv. Funct. Mater. 29 (2019), 1808522.
[3] J. Wu, Y. Cao, H. Zhao, J. Mao, Z. Guo, The critical role of carbon in marrying silicon and graphite anodes for high-energy lithium-ion batteries, Carbon Energy 1 (2019) 57–76.
[4] W. Shin, J. Lu, X. Ji, ZnS coating of cathode facilitates lean-electrolyte Li-S batteries, Carbon Energy 1 (2019) 165–172.
[5] R. Paul, Q. Dai, C. Hu, L. Dai, Ten years of carbon-based metal-free electrocatalysts, Carbon Energy 1 (2019) 19–31.
[6] S.L. Zhang, B.Y. Guan, X.F. Lu, S. Xi, Y. Du, X.W. Lou, Metal atom-doped Co_3O_4 hierarchical nanoplates for electrocatalytic oxygen evolution, Adv. Mater. 32 (2020), 2002235.
[7] C.Y. Chan, P.-K. Lee, Z. Xu, Y. Denis, Designing high-power graphite-based dual-ion batteries, Electrochim. Acta 263 (2018) 34–39.
[8] M. Li, C. Wang, Z. Chen, K. Xu, J. Lu, New concepts in electrolytes, Chem. Rev. 120 (2020) 6783–6819.
[9] J. Xu, Y. Dou, Z. Wei, J. Ma, Y. Deng, Y. Li, H. Liu, S. Dou, Recent progress in graphite intercalation compounds for rechargeable metal (Li, Na, K, Al)-ion batteries, Adv. Sci. 4 (2017), 1700146.
[10] M. Wang, Y. Tang, A Review on the features and progress of dual-ion batteries, Adv. Energy Mater. 8 (2018), 1703320.
[11] X. Yang, J. Luo, X. Sun, Towards high-performance solid-state Li-S batteries: from fundamental understanding to engineering design, Chem. Soc. Rev. 49 (2020) 2140–2195.
[12] I.A. Rodríguez-Pérez, X. Ji, Anion hosting cathodes in dual-ion batteries, ACS Energy Lett. 2 (2017) 1762–1770.
[13] L. Xiang, X. Ou, X. Wang, Z. Zhou, X. Li, Y. Tang, Highly concentrated electrolyte towards enhanced energy density and cycling life of dual-ion battery, Angew. Chem. Int. Ed. 59 (2020) 17924–17930.
[14] Y. Sui, C. Liu, R.C. Masse, Z.G. Neale, M. Atif, M. AlSalhi, G. Cao, Dual-ion batteries: the emerging alternative rechargeable batteries, Energy Storage Mater. 25 (2020) 1–32.
[15] X. Li, X. Ou, Y. Tang, 6.0 V High-voltage and concentrated electrolyte toward high energy density K-based dual-graphite battery, Adv. Energy Mater. 10 (2020), 2002567.
[16] T. Placke, A. Heckmann, R. Schmuch, P. Meister, K. Beltrop, M. Winter, Perspective on performance, cost, and technical challenges for practical dual-ion batteries, Joule 2 (2018) 2528–2550.
[17] T. Song, W. Yao, P. Kiadkhunthod, Y. Zheng, N. Wu, X. Zhou, S. Tunmee, S. Sattayaporn, Y. Tang, A low-cost and environmentally friendly mixed polyanionic cathode for sodium-ion storage, Angew. Chem. Int. Ed. 59 (2020) 740–745.
[18] K.V. Kravchyk, M.V. Kovalenko, Rechargeable dual-ion batteries with graphite as a cathode: Key challenges and opportunities, Adv. Energy Mater. 9 (2019), 1901749.
[19] N. Li, D. Su, In-situ structural characterizations of electrochemical intercalation of graphite compounds, Carbon Energy 1 (2019) 200–218.
[20] F. Liu, C. Wang, X. Sui, M.A. Riaz, M. Xu, L. Wei, Y. Chen, Synthesis of graphene materials by electrochemical exfoliation: recent progress and future potential, Carbon Energy 1 (2019) 173–199.
[21] C. Zhan, X. Zeng, X. Ren, Y. Shen, R. Lv, F. Kang, Z.-H. Huang, Dual-ion hybrid supercapacitor: integration of Li-ion hybrid supercapacitor and dual-ion battery realized by porous graphitic carbon, J. Energy Chem. 42 (2020) 180–184.
[22] A. Heckmann, O. Fromm, U. Rodehorst, P. Münster, M. Winter, T. Placke, New insights into electrochemical anion intercalation into carbonaceous materials for dual-ion batteries: impact of the graphitization degree, Carbon 131 (2018) 201–212.
[23] M.-C. Lin, M. Gong, B. Lu, Y. Wu, D.-Y. Wang, M. Guan, M. Angell, C. Chen, J. Yang, B.-J. Hwang, An ultrafast rechargeable aluminium-ion battery, Nature 520 (2015) 324–328.
[24] T. Placke, O. Fromm, S. Rothermel, G. Schmuelling, P. Meister, H.-W. Meyer, S. Passerini, M. Winter, Electrochemical intercalation of bis (trifluoromethanesulfonyl) imide anion into various graphites for dual-ion cells, ECS Trans. 50 (2013) 59–68.
[25] T. Placke, S. Rothermel, O. Fromm, P. Meister, S.F. Lux, J. Huesker, H.-W. Meyer, M. Winter, Influence of graphite characteristics on the electrochemical intercalation of bis (trifluoromethanesulfonyl) imide anions into a graphite-based cathode, J. Electrochem. Soc. 160 (2013) A1979–A1991.
[26] F. Wang, G. Chen, N. Zhang, X. Liu, R. Ma, Engineering of carbon and other protective coating layers for stabilizing silicon anode materials, Carbon Energy 1 (2019) 219–245.
[27] G. Zhang, X. Ou, C. Cui, J. Ma, J. Yang, Y. Tang, High-performance cathode based on self-templated 3D porous microcrystalline carbon with improved anion adsorption and intercalation, Adv. Funct. Mater. 29 (2019), 1806722.
[28] J. Peng, N. Chen, R. He, Z. Wang, S. Dai, X. Jin, Electrochemically driven transformation of amorphous carbons to crystalline graphite nanoflakes: a facile and mild graphitization method, Angew. Chem. 129 (2017) 1777–1781.
[29] L. Fan, Q. Liu, S. Chen, Z. Xu, B. Lu, Soft carbon as anode for high-performance sodium-based dual ion full battery, Adv. Energy Mater. 7 (2017) 1602778.
[30] I.-Y. Jeon, Y.-R. Shin, G.-J. Sohn, H.-J. Choi, S.-Y. Bae, J. Mahmood, S.-M. Jung, J.-M. Seo, M.-J. Kim, D.W. Chang, Edge-carboxylated graphene nanosheets via ball milling, PNAS 109 (2012) 5588–5593.
[31] I.-Y. Jeon, H.-J. Choi, S.-M. Jung, J.-M. Seo, M.-J. Kim, L. Dai, J.-B. Baek, Large-scale production of edge-selectively functionalized graphene nanoplatelets via ball milling and their use as metal-free electrocatalysts for oxygen reduction reaction, J. Am. Chem. Soc. 135 (2013) 1386–1393.
[32] H. Chen, F. Guo, Y. Liu, T. Huang, B. Zheng, N. Ananth, Z. Xu, W. Gao, C. Gao, A defect-free principle for advanced graphene cathode of aluminum-ion battery, Adv. Mater. 29 (2017), 1605958.
[33] A.D. Burrows, S.M. Cohen, Postsynthetic modification of coordination networks, CrystEngComm 14 (2012) 4095. -4095.
[34] J.L. Figueiredo, M. Pereira, M. Freitas, J. Orfao, Modification of the surface chemistry of activated carbons, Carbon 37 (1999) 1379–1389.
[35] M. Rosillo-Lopez, T.J. Lee, M. Bella, M. Hart, C.G. Salzmann, Formation and chemistry of carboxylic anhydrides at the graphene edge, RSC Adv. 5 (2015) 104198–104202.
[36] M. Rosillo-Lopez, C.G. Salzmann, A simple and mild chemical oxidation route to high-purity nano-graphene oxide, Carbon 106 (2016) 56–63.
[37] B. Gupta, N. Kumar, K. Panda, V. Kanan, S. Joshi, I. Visoly-Fisher, Role of oxygen functional groups in reduced graphene oxide for lubrication, Sci. Rep. 7 (2017) 1–14.
[38] S. Kellici, J. Acord, J. Ball, H.S. Reehal, D. Morgan, B. Saha, A single rapid route for the synthesis of reduced graphene oxide with antibacterial activities, RSC Adv. 4 (2014) 14858–14861.
[39] A.E.D. Mahmoud, A. Stolle, M. Stelter, Sustainable synthesis of high-surface-area graphite oxide via dry ball milling, ACS Sustainable Chem. Eng. 6 (2018) 6358–6369.
[40] X. Zhang, Y. Tang, F. Zhang, C.S. Lee, A novel aluminum-graphite dual-ion battery, Adv. Energy Mater. 6 (2016), 1502588.
[41] P. Meister, O. Fromm, S. Rothermel, J. Kasnatscheew, M. Winter, T. Placke, Sodium-based vs. lithium-based dual-ion cells: electrochemical study of anion intercalation/de-intercalation into/from graphite and metal plating/dissolution behavior, Electrochim. Acta 228 (2017) 18–27.
[42] W. Li, A. Dolocan, P. Oh, H. Celio, S. Park, J. Cho, A. Manthiram, Dynamic behaviour of interphases and its implication on high-energy-density cathode materials in lithium-ion batteries, Nat. Commun. 8 (2017) 1–10.
[43] Q. Chen, Y. Pei, H. Chen, Y. Song, L. Zhen, C.-Y. Xu, P. Xiao, G. Henkelman, Highly reversible oxygen redox in layered compounds enabled by surface polyanions, Nat. Commun. 11 (2020) 1–12.
[44] Y. Qiao, K. Jiang, X. Li, H. Deng, Y. He, Z. Chang, S. Wu, S. Guo, H. Zhou, A hybrid electrolytes design for capacity-equivalent dual-graphite battery with superior long-term cycle life, Adv. Energy Mater. 8 (2018), 1801120.
[45] J.A. Read, A.V. Cresce, M.H. Ervin, K. Xu, Dual-graphite chemistry enabled by a high voltage electrolyte, Energy Environ. Sci. 7 (2014) 617–620.
[46] Y. Wang, S. Wang, Y. Zhang, P.-K. Lee, D.Y. Yu, Unlocking the true capability of graphite-based dual-ion batteries with ethyl methyl carbonate electrolyte, ACS Appl. Energy Mater. 2 (2019) 7512–7517.

[47] H. Fan, L. Qi, H. Wang, Intercalation behavior of hexafluorophosphate into graphite electrode from propylene/ethylmethyl carbonates, J. Electrochem. Soc. 164 (2017) A2262–A2267.
[48] P. Li, Z. Fang, Y. Zhang, C. Mo, X. Hu, J. Jian, S. Wang, D. Yu, A high-performance, highly bendable quasi-solid-state zinc–organic battery enabled by intelligent proton-self-buffering copolymer cathodes, J. Mater. Chem. A 7 (2019) 17292–17298.
[49] G. Wang, M. Yu, J. Wang, D. Li, D. Tan, M. Löffler, X. Zhuang, K. Müllen, X. Feng, Self-activating, capacitive anion intercalation enables high-power graphite cathodes, Adv. Mater. 30 (2018), 1800533.
[50] X. Zhao, H. Xu, Z. Hui, Y. Sun, C. Yu, J. Xue, R. Zhou, L. Wang, H. Dai, Y. Zhao, Electrostatically assembling 2D nanosheets of MXene and MOF-derivatives into 3D hollow frameworks for enhanced lithium storage, Small 15 (2019), 1904255.
[51] Y. Wang, J. Li, Y. Huang, H. Wang, Anion storage behavior of graphite electrodes in $LiBF_4$/sulfone/ethyl methyl carbonate solutions, Langmuir 35 (2019) 14804–14811.
[52] J. Zou, C. Sole, N.E. Drewett, M.J. Velický, L.J. Hardwick, In situ study of Li intercalation into highly crystalline graphitic flakes of varying thicknesses, J. Phys. Chem. Lett. 7 (2016) 4291–4296.
[53] C. Song, Y. Li, H. Li, T. He, Q. Guan, J. Yang, X. Li, J. Cheng, B. Wang, A novel flexible fiber-shaped dual-ion battery with high energy density based on omnidirectional porous Al wire anode, Nano Energy 60 (2019) 285–293.
[54] C.M. Julien, A. Mauger, In situ Raman analyses of electrode materials for Li-ion batteries, AIMS Mat. Sci. 5 (2018) 650–698.
[55] N. Li, F. Zhang, Y. Tang, Hierarchical T-Nb_2O_5 nanostructure with hybrid mechanisms of intercalation and pseudocapacitance for potassium storage and high-performance potassium dual-ion batteries, J. Mater. Chem. A 6 (2018) 17889–17895.

Maiwen Zhang received her bachelor degree (2017) in Chemical Engineering Department at East China University of Science and Technology. She is now a Ph.D candidate at the Department of Chemical Engineering in University of Waterloo under supervision of Prof. Aiping Yu. She mainly works on nanomaterials investigation for dual-ion batteries, zinc-ion batteries and supercapacitors.

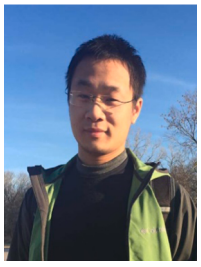

Yi Pei is a post-doctoral at the Department of Chemical Engineering, University of Waterloo, under supervision of Prof. Zhongwei Chen. He received his bachelor degree in 2012 and Ph.D. degree in 2017 from Harbin Institute of Technology (HIT). He has been a joint Ph.D student in the group of Prof. Guozhong Cao at the University of Washington at Seattle (UW) from 2014 to 2016. His research interests focus on cathode materials for rechargeable batteries, especially for Li, Na, Zn and Dual-ion batteries.

Wenwen Liu received his Ph.D. degree (2020) in Department of Chemical Engineering under the supervision of Prof. Aiping Yu at the University of Waterloo. He mainly focuses on nanomaterials designing and construction of electrochemical energy storage devices and electrocatalysts.

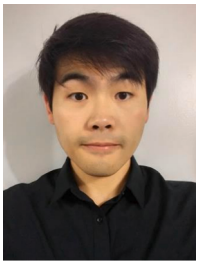

Ruilin Liang received his M.A.Sc degree (2019) in Chemical Engineering and Nanotechnology under the supervision of Prof. Zhongwei Chen at University of Waterloo, Waterloo, Canada, where he specialized in rechargeable Zn-MnO_2 batteries. He is currently working as a research engineer, focusing on the development of hydrogen fuel cell.

Ya-Ping Deng received his Ph.D. degree (2020) in Chemical Engineering under the supervision of Prof. Zhongwei Chen at University of Waterloo. He is now a postdoctoral researcher in Prof. Chen group. His research currently focusses on the exploration of novel electrode materials and solid-state electrolytes for lithium-ion batteries and rechargeable metal-air batteries.

Dr. Zhongwei Chen received his Ph.D. from the University of California, Riverside in 2007. He is Canada Research Chair Professor in Advanced Materials for Clean Energy at the University of Waterloo, a Fellow of the Canadian Academy of Engineering and Vice President of International Academy of Electrochemical Energy Science (IAOEES). His research mainly includes advanced nanomaterials development for energy storage devices such as lithium ion batteries, fuel cells and metal-air batteries.

Dr. Aiping Yu is a professor in the Department of Chemical Engineering at the University of Waterloo, Ontario, Canada. She obtained her Ph.D. in 2007 from the University of California, Riverside. She mainly focuses on the application of carbon-based nanomaterials on photocatalysts and energy storage devices including micro-supercapacitors, metal-air batteries, lithium ion batteries and dual-ion batteries.